[1]Department of Marine Earth and Atmospheric Sciences, North Carolina State University, Raleigh, North Carolina, U.S.A
[2]Naval Research Laboratory, Washington, D.C., U.S.A.
[3]Naval Research Laboratory, Monterey, California, U.S.A.

A Non-Hydrostatic Modeling Study of Surface Moisture Effects on Mesoscale Convection Induced by Sea Breeze Circulation

L. Xu[1], **S. Raman**[1], **R. V. Madala**[2], and **R. Hodur**[3]

With 17 Figures

Summary

Convection and subsequent precipitation induced by the sea breeze circulations are often observed in the Florida peninsula during summer. In this study, the mechanisms of initiation and maintenance of the convective clouds and precipitation are investigated. A fully-compressible fine resolution non-hydrostatic mesoscale numerical model is used in this study. Surface energy and moisture budget were included in this model to simulate the diurnal cycle of ground surface temperature and wetness. The model also has a sophisticated boundary layer and explicit cloud physics. A sounding obtained from Orlando, Florida at 1110 UTC 17 July 1991 as part of the Convection and Precipitation Electrification (CaPE) experiment is used for initialization. The initial data for the model is kept in geostrophic and thermal wind balance. Several sensitivity tests were conducted to investigate the effects of different treatments of ground surface moisture and temperature on the model forecast of the convection and precipitation induced by the sea breeze circulations. The simulations agree reasonably well with the observations when both surface energy and moisture budget were included in the model to predict ground surface temperature and wetness. The surface moisture has a significant impact on the formation, strength, sustenance, and the location of convection and precipitation induced by the sea breezes.

1. Introduction

Surface latent and sensible heat fluxes are two key elements in the initiation and maintenance of sea breeze circulations although the ambient wind, and the atmospheric stability also play a role. The primary driving force for the sea breeze circulation is the heating over the land surface. Thus it is very important to predict the ground surface temperature correctly in the model. Generally, two different methods are used to obtain the ground surface temperature in the model. It is either specified as a time dependent sinusoidal wave (Pielke, 1974; Tapp and White, 1976; Mahfouf et al., 1987), or predicted (Bougeault, 1987; Nicholls et al., 1991).

The influence of surface moisture on the sea breeze circulation over the Florida peninsula has been the subject of several numerical studies (McCumber, 1980; Nicholls et al., 1991). A three-dimensional hydrostatic model coupled with a multilayered soil model was used in a study by McCumber (1980) to investigate the effect of surface fluxes on the sea breeze circulations. A two-dimensional non-hydrostatic model was used by Nicholls et al. (1991) to perform sensitivity tests for a variety of wind and thermodynamic profiles, and for different soil moisture contents.

The Convective and Precipitation Experiment (CaPE) was conducted in the central Florida region during the period, 8 July through 18 August 1991. Two of the five main objectives of CaPE as indicated in Williams et al. (1992) are: a) development of mesoscale numerical forecast (2–12 hour)

of wind, clouds, and thunderstorms; and b) improving techniques for performing short period forecasts of convection initiation, downburst, and tornadoes.

The sea breeze circulation is due to the thermal contrast between land and ocean. This thermal contrast produces differences in both the latent and the sensible heat fluxes. Realistic simulation of the sea breeze circulation, requires proper simulation of the surface fluxes. The goals of this study are 1) to examine whether a three-dimensional non-hydrostatic model is capable of reproducing the sea breeze circulation, deep convection and associated precipitation observed on 17 July 1991 CaPE; and, 2) to determine the sensitivity of the convection and the precipitation to soil moisture content.

A brief description of the non-hydrostatic model is given in Section 2. Observations on 17 July 1991 during CaPE are presented in Section 3. The numerical experiments used in this study are described in Section 4 along with a discussion of the results. Summary and conclusions are given in Section 5.

2. The Model

The atmospheric part of the Coupled Ocean/Atmospheric Mesoscale Prediction System (COAMPS), developed at the Naval Research Laboratory (Hodur, 1993), is used in this study. COAMPS features a non-hydrostatic atmospheric model coupled to a hydrostatic ocean model. A brief description of the atmospheric model is given below. More detailed description of the COAMPS is given by Hodur (1993).

The fully-compressible Navier-Stokes equations are written in a manner similar to that used by Klemp and Wilhelmson (1978). The turbulence closure uses a $e - l$ closure, where e is the turbulent kinetic energy and l is the mixing length determined diagnostically. An explicit five phase cloud physics scheme suggested by Rutledge and Hobbs (1983) is used for determining the cloud processes. The variables predicted in the atmospheric part of COAMPS are: the wind component u, v and w in the x-, y- and z-directions, respectively, the perturbation of the Exner function π, the potential temperature θ, the turbulent kinetic energy e, and the mixing ratios of water vapor, cloud water, rain water, ice crystals and snowflakes q_v, q_c, q_r, q_i and

q_s, respectively. The Exner function is defined as: $\pi = (p/p_{00})^{R_d/C_p}$.

Since diurnal changes of ground temperature and wetness are important in determining the sensible and the latent heat fluxes, two prognostic equations for the ground temperature T_g and ground moisture W_g were added to the COAMPS to make it suitable for this study. The variables T_g and W_g are predicted following Louis et al. (1979):

$$\frac{\partial T_g}{\partial t} = (F_R - F_H - LF_W)/C_T + (T_d - T_g)/\tau, \quad (1)$$

$$\frac{\partial W_g}{\partial t} = (P - F_W)/C_W + (W_d - W_g)/\tau, \quad (2)$$

with

$$W_g \leqslant W_{max}. \quad (3)$$

Here F_R, F_H and F_W are the fluxes of net radiation, sensible heat and water vapor, respectively (positive upwards); P is precipitation; T_d and W_d are the values of the temperature and moisture of the deep layer in the ground; C_T and C_W are the capacities for heat and moisture of the superficial layer that reacts to the diurnal heating cycle, and τ is the time scale for the restoring effect of the deep layer. After the soil moisture reaches W_{max}, any excess water is eliminated by run-off. The mixing ratio at the ground surface q_0 is related to the soil moisture and temperature:

$$q_0 = W_g q_{sat}(T_g)/W_{max}. \quad (4)$$

The constants used in (1)–(4) are the same as the ones used by Louis et al. (1979).

A finite difference method is used to solve the governing equations in Cartesian coordinate system. Staggered, C grid (Arakawa and Lamb, 1977) is used in horizontal. All the derivatives are computed to second-order accuracy except the horizontal diffusion, which uses fourth-order accuracy to damp only the shortest wavelengths.

One of the difficulties associated with a fully compressible non-hydrostatic system is that the system allows for the existence of a full spectrum of wave motions including the high frequency acoustic waves. The acoustic waves contain small amounts of energy and are not meteorologically important, but they require a very small time step due to their high propagation speed. There are two methods to deal with the acoustic modes in a fully-compressible, non-hydrostatic system (Xu

et al., 1992). One is the semi-implicit scheme and the other is the time-split technique.

The semi-implicit scheme was developed in the late 60's (Robert, 1969) to allow time steps larger than those in a conventional explicit time integration of a primitive equation model. Larger time steps are achieved by a substantial slowing of fast moving gravity waves. The idea behind the semi-implicit scheme is to treat the dominant terms that govern the acoustic modes in the equation of motion implicitly. On the other hand, the time-splitting scheme commonly used in compressible nonhydrostatic models contains two main steps. The forcing terms are separated into two types, namely, those that govern linear acoustic modes and all the other terms. Smaller time steps are used for terms that govern acoustic waves, while larger time steps are used for all the other terms. Note that the smaller time steps are not necessary for the thermodynamic, moisture and turbulent kinetic energy equations. The time-splitting technique introduced by Klemp and Wilhelmson (1978) is used for time integration of both u-component and v-components of momentum equations in COAMPS.

The subgrid scale mixing in vertical is parameterized using the level-2 method of Mellor and Yamada (1974). The subgrid scale mixing in horizontal is based on the deformation of the horizontal velocity field (Smagorinsky, 1963). A radiation type lateral boundary condition similar to that proposed by Orlanski (1976) is used. The upper and the lower boundaries require specification of the vertical velocity and fluxes. In this model version, we set $w = 0$ at both the upper and lower boundaries. The lower boundary conditions on the vertical mixing terms are determined using the surface flux parameterization by Louis et al. (1982). At the upper boundary, the normal gradient of the vertical mixing terms is assumed to vanish to prevent the development of unrealistic tendencies. High-frequency time oscillations arise due to spurious modes generated by the leapfrog scheme. These are smoothed by using a time filter suggested by Robert (1966). A smoothing parameter of 0.2 is used.

The model domain covers the whole Florida peninsula and its surrounding oceans and is 600 km by 700 km in horizontal and 10 km in vertical. There are 61 and 71 grid points in x and y directions respectively with an uniform grid interval of 10 km, and 28 levels in the vertical direction. Vertical grid intervals vary from 100 m near the surface to 700 m near the top of the domain. A land-sea table is used to separate land from the ocean in the model. The coastline is indicated by a thick line in all the horizontal figures. Large and small time steps are 90 s and 30 s, respectively.

3. Observations

The day chosen for this study is 17 July 1991 during CaPE. One reason for the selection of this day is the presence of a weak synoptic forcing. According to Williams et al. (1992), the synoptic scale features at 1200 UTC included an upper-air trough located in Alabama which drifted slowly westward. The east-west Atlantic ridge moved northward and the low-level flow backed to the south-southeast almost parallel to the coastline. A brief description of the significant weather observed on July 17, 1991 given below is based on the "CaPE Operations Summary and Data Inventory" by Williams et al. (1992).

Figure 1 shows the locations where significant weather events, such as strong winds, deep convection, heavy precipitation, occurred on July 17, 1991. Initial convection occurred in the sea breeze zone along the east coast which moved northwestward. Convection developed in the area west of Melbourne to near Vero Beach (1900–2000 UTC). Thunderstorm wind gusts (1930 UTC) of 78 mph downed trees in Dunnellon. Strong thunderstorm winds (2100–2130 UTC) uprooted trees and downed power lines near Plant city. Three funnel clouds (2156 UTC) were reported near Lakeland. Large size hail (2220 UTC) fell briefly at Auburndale, 10 miles east of Lakeland. A funnel cloud (2225 UTC) briefly touched down in an open field near Lake Wales. Thunderstorm winds (2305 UTC) downed trees and power lines in Dade City. A 0.7 inch hourly precipitation (2100 UTC) was observed in Raiford, in northern Florida. A 0.7 inch hourly precipitation (2300 UTC) was observed in Saint Leo, north of Tampa Bay. Since there were no large scale disturbances in the region, it is believed that all the convective activities were mainly due to the local forcing caused by sea breeze circulations. To further examine the evolution of the sea breeze circulations, digitized visible satellite images representing reflection from the clouds over the CaPE area are presented here.
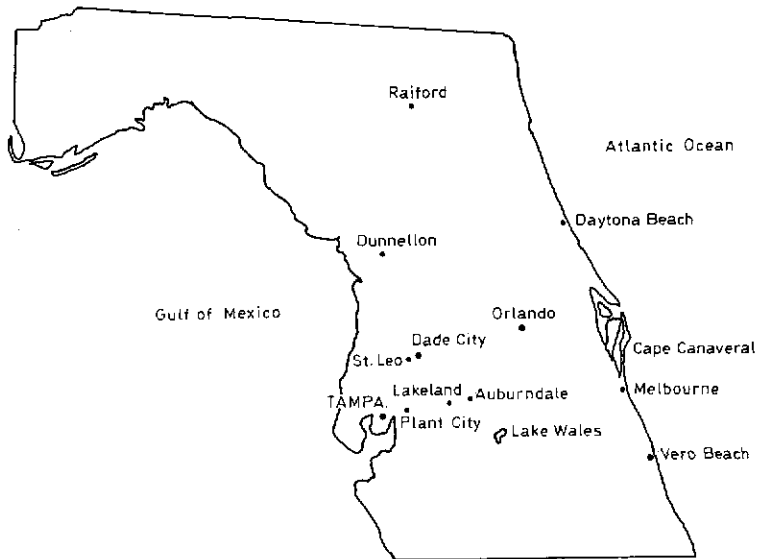
Fig. 1. Central Florida where CaPE was con-
ducted. Model domain included parts of Gulf of
Mexico and the Atlantic Ocean

The visible satellite images displayed a clear sky
over the peninsula at 1100 UTC (not shown). By
1400 UTC, the intensity of the reflections over the
east coast was about 100 (weak convection) in the
digitized satellite image as indicated in Fig. 2a.
The region with weak convection was mainly over
south of Cape Canaveral. At 1700 UTC, scattered
convection with an intensity of reflection of about
180 (moderate convection) can be seen in the
northern and eastern parts of Florida as shown in
Fig. 2b. As indicated in Fig. 2c, intensity of the
reflection reached to a value, more than 200
(strong convection) over a location north of Lake
Okeechobee and near Dunnellon around 2000
UTC. The convection, however, decayed in the
east coast, but intensified in the west coast by 2200
UTC (Fig. 2d).

Wind and thermodynamic profiles (Fig. 3) used
in this study are from the sounding at 1110 UTC
from Orlando, Florida for 17 July 1991 during
CaPE. The initial data for the model were kept in
geostrophic and thermal wind balance. The surface
temperature is taken to be the same for both land
and ocean at 1110 UTC. The surface temperature
over water is held constant for all the experiments.

4. Discussion of Results

Three numerical experiments are performed using
the same initial conditions but with different soil
moisture contents. Experiment 1 (EXP1) is design-
ed to simulate the 17 July 1991 case over the
Florida peninsula with full model physics. EXP1

served as the control simulation. Experiment 2
(EXP2) is the same as EXP1 except that the ratio
of W_g/W_{max} is assumed to be unity. EXP2 is
designed to investigate the effect of saturated
ground surface on sea breeze circulation. Experi-
ment 3 (EXP3) is the same as EXP1 except what
W_g is set to zero (dry condition). To isolate the
effect of surface forcing, the atmospheric radiation
transfer is turned off for all the experiments.

4.1 Experiment 1: Control Simulation

4.1.1 Horizontal Structures

The simulated wind fields at 55 m height at
different integration times are shown in Fig. 4a to
4c. They display the evolution of the sea breeze
circulations at both the coasts. The sea breeze
started developing along the coastal regions at 6 h
(Fig. 4a). The maximum wind speed is about
$8 ms^{-1}$ in Fig. 4a. Penetration of the sea breeze is
relatively weak at 6 h. By 9 h, however, two well
defined sea breeze convergence zones are present
as apparent in Fig. 4b. The maximum wind speed
by this time is about 12 ms^{-1}. The lake effect at
9 h can be seen in the wind field. The sea breeze
circulation is well developed at 9 h. The low level
wind pattern at 12 h is shown in Fig. 4c. Now, the
maximum surface wind speed of 14 m/s is located
northeast of Tampa Bay, which is consistent with
the observed strong thunderstorm wind near
Dade City (see Fig. 1). Due to the effect of the
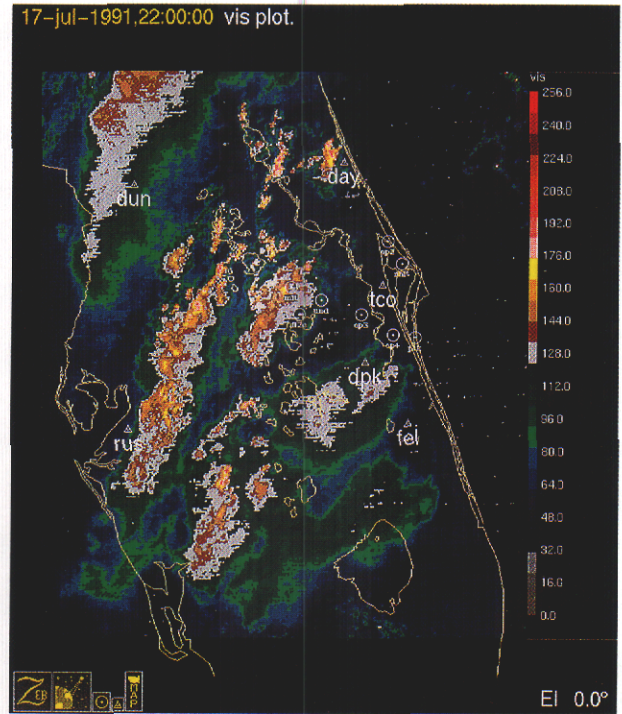outflows caused by the thunderstorms, the sea
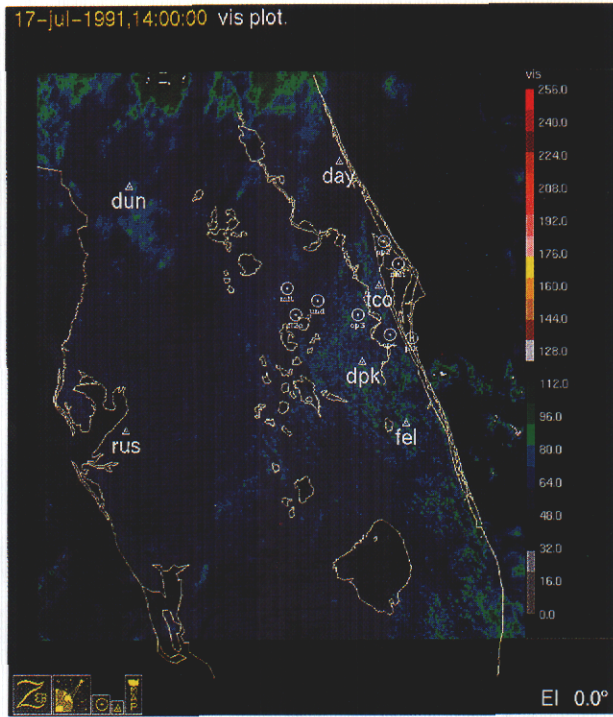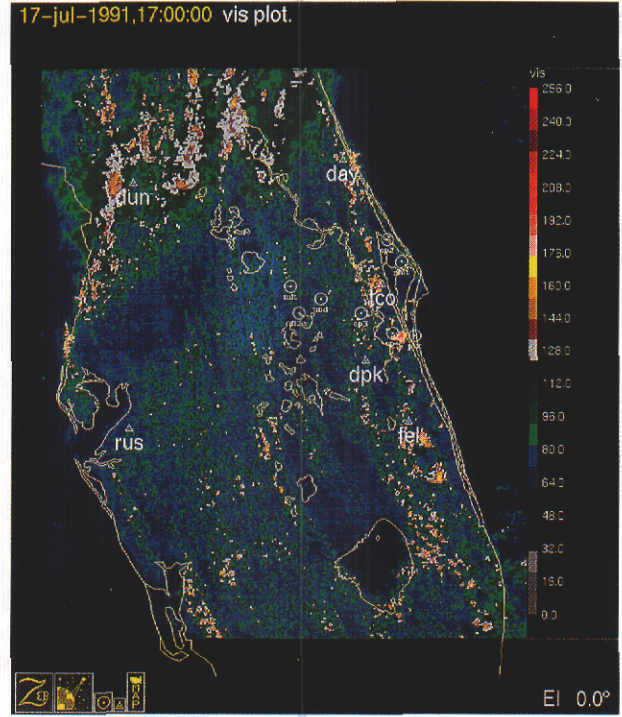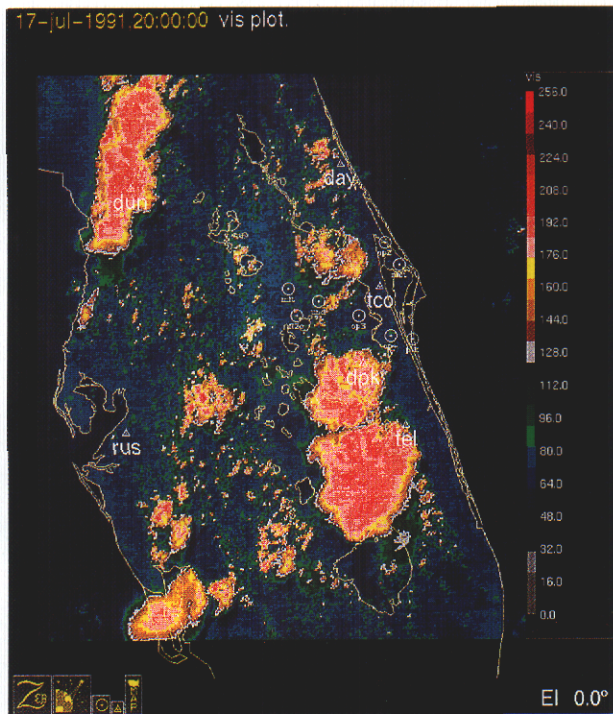
Fig. 2. The visible satellite images over Florida. The legend indicates the degree of reflectance. The hot colors (reds) indicate deep convection and the cold colors (blues) indicate clear sky and weak convection. (a) 1400 UTC 17 July 1991, (b) 1700 UTC 17 July 1991, (c) 2000 UTC 17 July 1991, and (d) 2200 UTC 17 July 1991
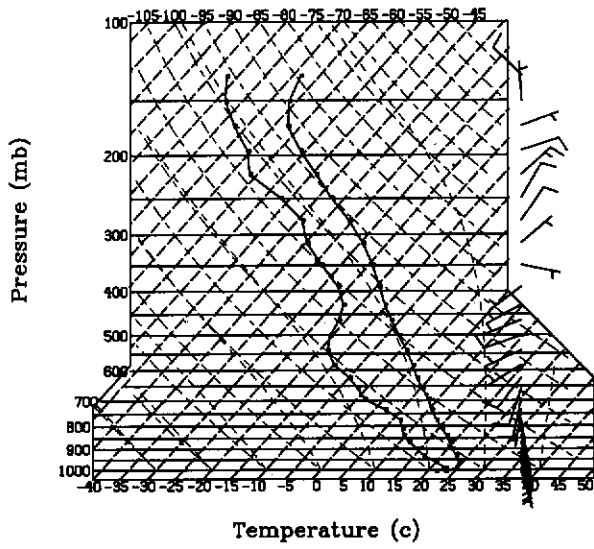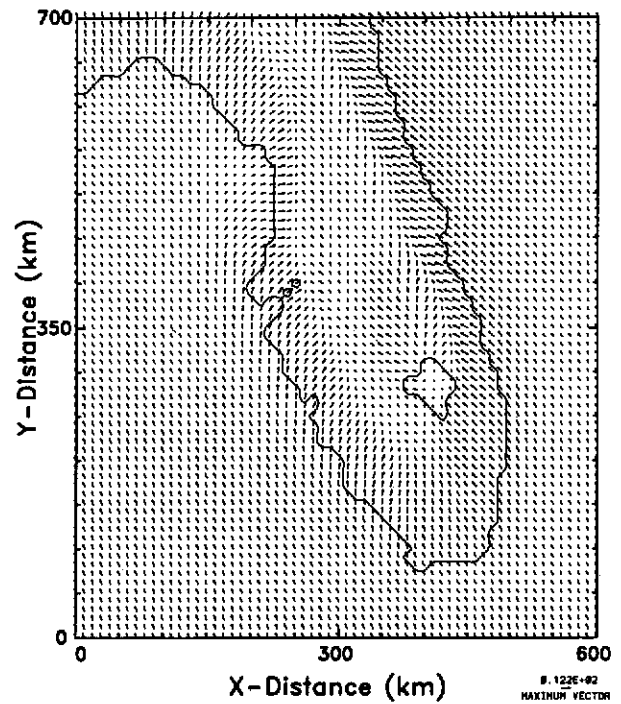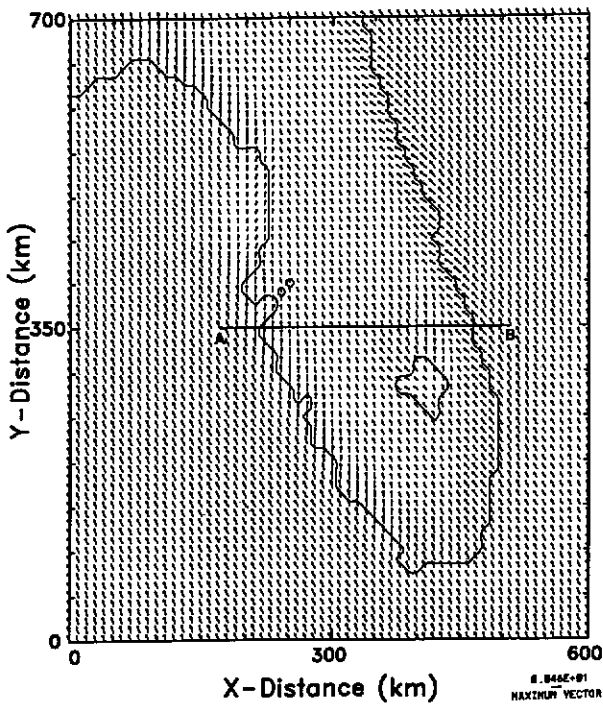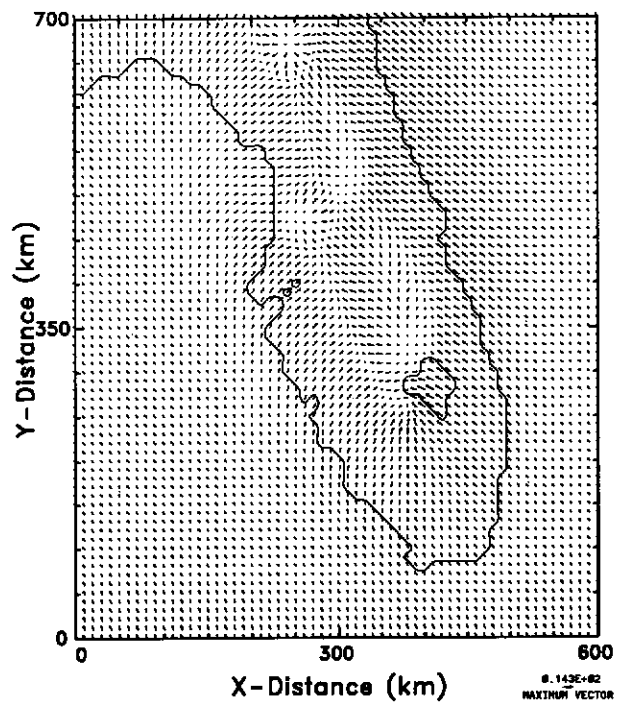
Fig. 3. The sounding at 1110 UTC from Orlando, Florida for 17 July 1991 during CaPE used to initialize the model. The dew point, temperature, and wind bar are presented. Wind direction varied from southeasterly between surface and 800 mb, southwesterly between 800 mb and 400 mb, and northeast above 400 mb


b

a

c

Fig. 4. The model predicted horizontal wind fields (in m s^{-1}) at 55 m height from EXP1 are superposed with a contour of land-sea table, which separates land from water. (a) 6 h horizontal wind field. The maximum wind speed is about 8.5 m s^{-1}. The line AB indicates the location of cross sections used later. (b) 9 h horizontal wind field. The maximum wind speed is 12.2 m s^{-1}. (c) 12 h horizontal wind field. The maximum wind speed is 14.3 m s^{-1}

breeze convergence zones in Fig. 4c are no longer well defined.

Since the sea breeze is a result of the thermal gradients caused by the uneven heating over the land and the ocean, an examination of the simulated ground temperature fields will be of interest. Ground temperature deviation (GTD) is used as an indicator of the increase in temperature. This is obtained as a difference between the predicted ground temperature and corresponding initial value. A strong gradient in the 6 h GTD field is present along the Florida coastline (Fig. 5a). This strong gradient is a result of the differential heating over land and ocea. The ground temperature difference between land and ocean is about 10 °C. Two relatively large GTD zones with values larger than 13 °C are present over both the coasts. The coastal regions with relatively small GTD at this hour correspond to the locations at which the sea breeze induced surface convergences occur (see Fig. 4a).
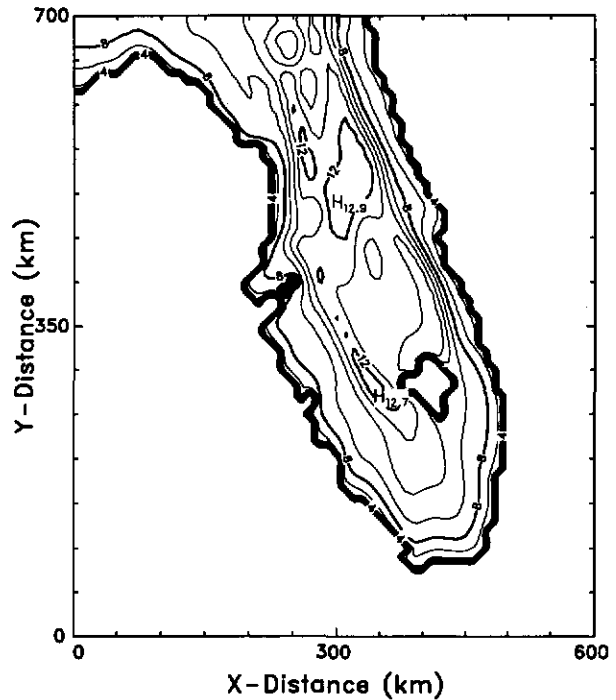
Ground temperature deviations predicted at 9 h are shown in Fig. 5b. The discontinuity of GTD along the coastline is still present at this hour. The maximum value of GTD reaches to about 16 °C near Dunnellon (Fig. 1) at this hour. Also, maximum values of GTD are present over the western parts of the central and northern Florida. The
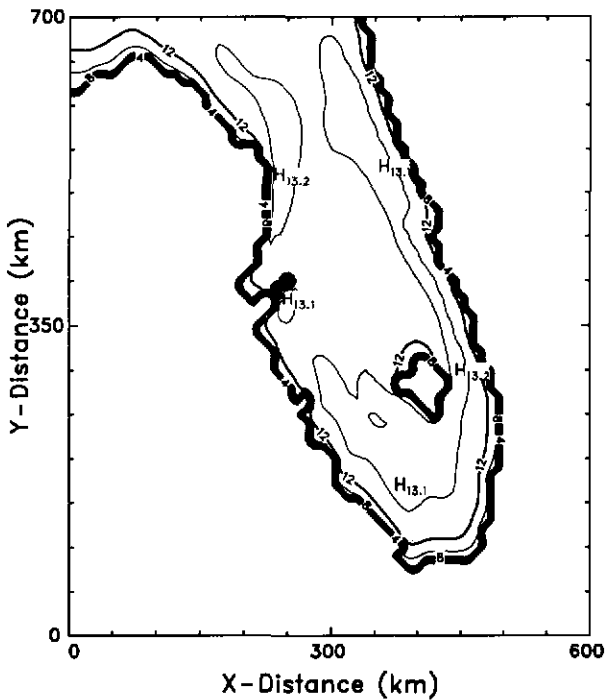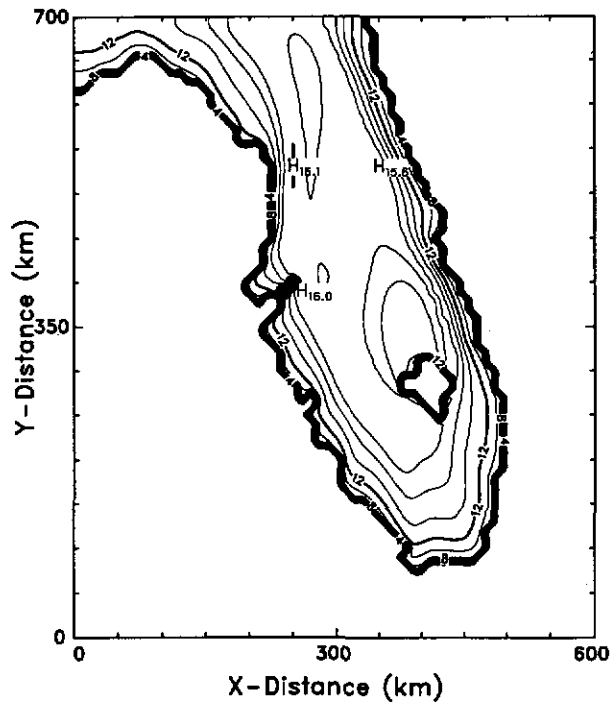
b

c

Fig. 5. Simulated ground temperature deviations (in °C) from EXP1, at (a) 6 h simulation, (b) 9 h simulation and (c) 12 h simulation. The ground temperature deviation is obtained by subtracting the initial ground temperature from the simulated temperature. A contour interval of 1 °C is chosen

a

cooling due to the sea breeze circulations extends further inland at 9 h. A relatively colder region exists downwind of the lake Okeechobee. This colder region is believed to have been caused by the cold air advection from the lake.

Less GTD gradients are found along both the coasts at 12 h (Fig. 5c). The maximum value of GTD at 12 h is about 3 °C smaller as compared to the one at 9 h. The GTD field is now more complex. Note that there are two cool spots in GTD field: the first one is located near Raiford in the northern Florida (see Fig. 1), and the second one is near St Leo, north of Tampa Bay (see Fig. 1). These two cold spots have been caused by the thunderstorm outflows indicated in Fig. 4c. The outflows are caused by strong horizontal temperature gradients produced by the evaporative cooling of rain water in an unsaturated environment.

The distribution of the 12 h accumulated precipitation is shown in Fig. 6. The model simulated a maximum of about 5.1 cm accumulated rainfall near Raiford in northern Florida as compared to the observed hourly precipitation of about 2 cm (2100 UTC); a maximum of about 4.6 cm accumulated precipitation about 75 km northeast of Tampa Bay as compared with the observed hourly
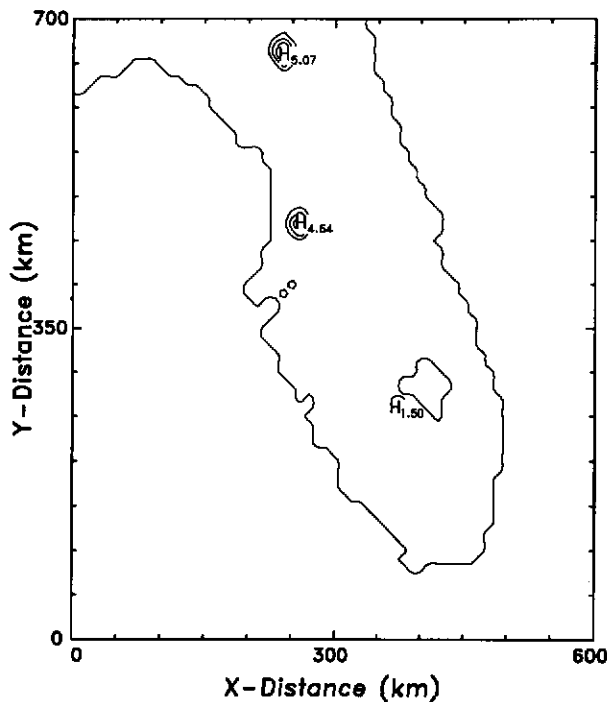
precipitation of about 2 cm at Saint Leo (2300 UTC); and a maximum of 1.5 cm over the southwest side of lake Okeechobee. There is a reasonable agreement between the predicted rainfall and the observations considering that the model values are accumulated precipitation over 12 h whereas the observation are hourly. Also sparse precipitation measurements make it difficult to compare more quantitatively. The satellite pictures (Fig. 2) do indicate cloud coverage over the west coast between 2000–2300 UTC. This result is also consistent with a two-dimensional study by Nicholls et al. (1991), where they found that the precipitation occurred mainly near the west coast for easterly ambient wind.

4.1.2 Vertical Structures

To further investigate the evolution of the sea breeze circulation and the associated convection, east-west cross sections along the line $\overline{AB}$ indicated in Fig. 4a are examined. The u-component predicted at 6 h is shown in Fig. 7a. The sea breeze circulation has reached to about 3 km height at both the east and the west coasts. The magnitude of the easterly wind component is more than 4 m s^{-1} over the east coast at low levels. A relatively weak westerly wind is present near the west coast at low levels. The sea breeze circulation is relatively weak at 6 h. By 9 h, however, the sea breeze circulation is much stronger and reaches to about 5.3 km as shown in Fig. 7b. Convergence zones are present near the east and the west coasts to a height of about 2 km, and divergence zones aloft between 2 km and 5.3 km. The return flows are
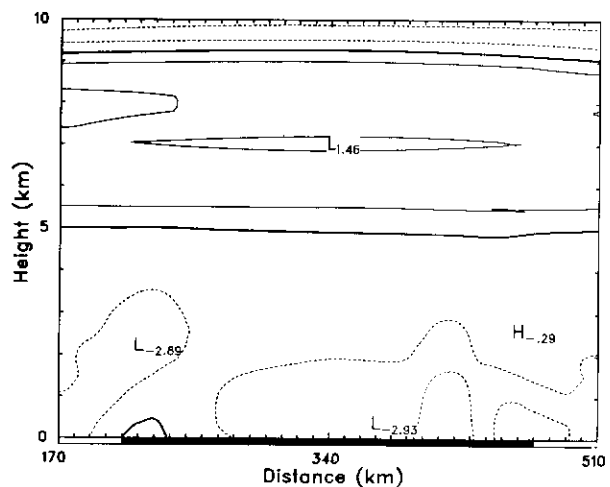
Fig. 6. Accumulated precipitation (in cm) during 12 h integration with contour interval of 1 cm

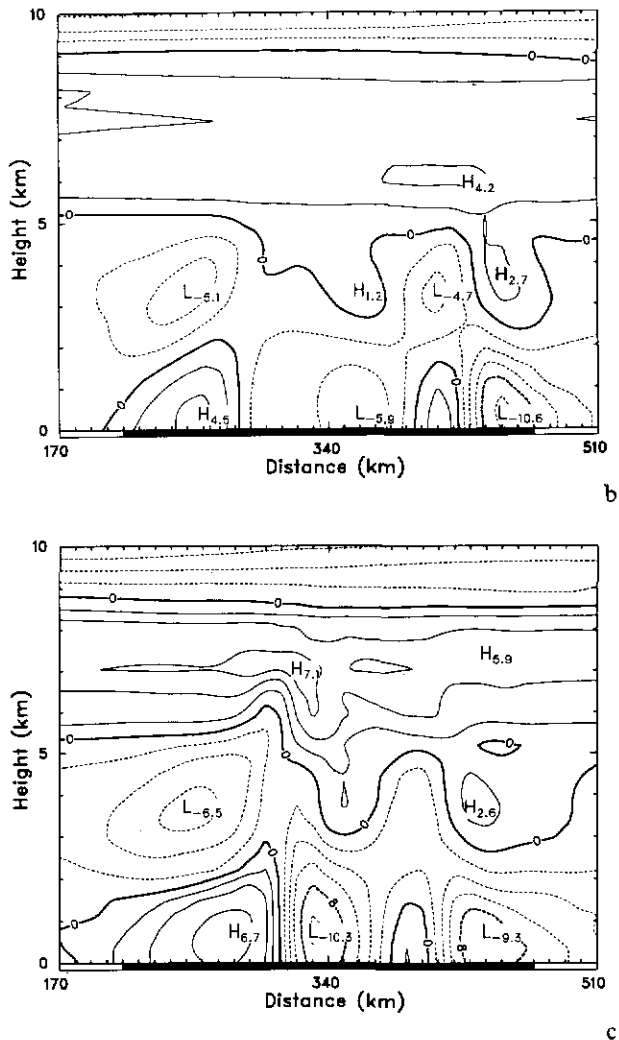Fig. 7. (Continued)   a

b

c

Fig. 7. Cross sections of the simulated u-component (in $m s^{-1}$) from EXP1 along the AB as indicated in Fig. 4a, at (a) 6 h simulation, (b) 9 h simulation, and (c) 12 h simulation. The land portion of the figures are marked with heavier lines. The contour interval used here is $2 m s^{-1}$

apparent over both the coasts at a height of about 3.5 km. Maximum value of the westerly wind component over the west coast at low levels is $4.5 m s^{-1}$. Maximum westerly wind component now occurs at about 30 km east of the corresponding location at 6 h. This implies that the sea breeze circulation over the west coast has extended further inland. The maximum value of the easterly wind component near the east coast at low levels is $10.6 m s^{-1}$. The center of the maximum easterly wind component at low levels is now located at about 20 km west of the one predicted at 6 h. This indicates that the sea breeze circulation over the

east coast moves slower inland as compared to the one over the west coast. This appears to be due to the Coriolis effect of the strong southerly component of the ambient wind. Stronger convergence over the east coast at 9 h is consistent with the strong reflection by the clouds indicated by the satellite imagery (Fig. 2c) over the east coast.

The sea breeze circulation at 12 h reaches to about 7 km as shown in Fig. 7c. The maximum value of the low level westerly wind component reaches to about $6.7 m s^{-1}$ over the west coast. The maximum value of the low-level easterly wind component, however, decreases to about $9.3 m s^{-1}$. The sea breeze circulation extends further inland over the west coast than over the east coast. Low level convergence over the west coast is also stronger than the one over the east coast at this hour due to vigorous deep convection. This result is consistent with the stronger reflection on the satellite imagery over the west coast. Overall, the sea breeze circulation is stronger over the west coast than over the east coast at 12 h simulation.

Cross sections of simulated vertical velocities at 6 h, 9 h and 12 h are shown in Fig. 8a, 8b, and 8c respectively. The vertical motions are relatively weak in general at 6 h (Fig. 8a). There are two major upward and downward motion zones; one over the east coast and the other over the west coast, the former being stronger. The maximum values of the upward and downward vertical velocities are $6 cm s^{-1}$ and $4 cm s^{-1}$, respectively over the east coast. The maximum values of the upward and downward motions are only $4 cm s^{-1}$ and $2 cm s^{-1}$, respectively over the west coast. A secondary upward motion zone with a maximum value of about $1 cm s^{-1}$ is located near the middle of the peninsula.

The two major upward motion zones have moved further inland and have extended to higher elevations (Fig. 8b). The upward motion in the east coast is still stronger than the one in the west coast. The maximum values of the upward motion over the east and the west coasts are more than $42 cm s^{-1}$ and $23 cm s^{-1}$, respectively. The $10 cm s^{-1}$ contour lines reach a higher altitude over the east coast as compared to the west coast. The upward motion is over a narrow region over the east coast as compared to the west coast and the convection is in general stronger over the east coast. This result is consistent with the observed convective activities in the area between Melbourne and Vero Beach
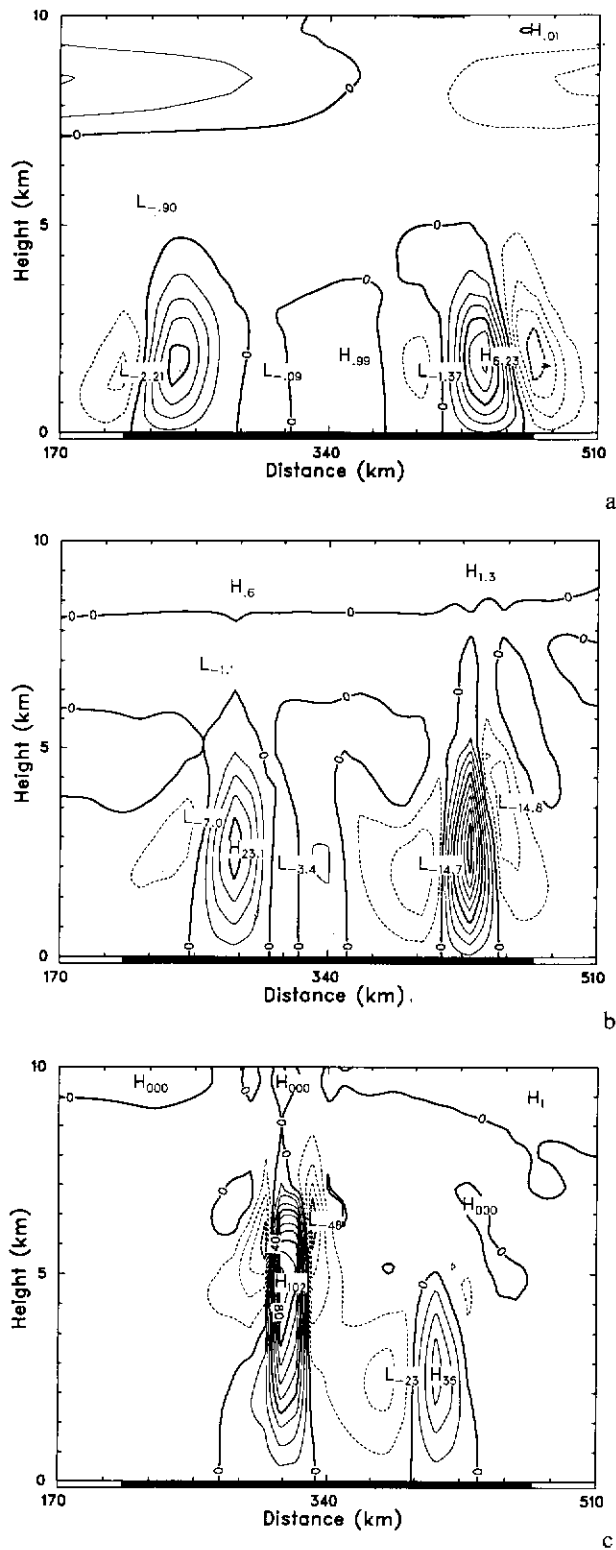
Fig. 8. Cross sections of the simulated w-component (in cm s^{-1}) from EXP1 along line AB as indicated in Fig. 4a, at (a) 6 h simulation, (b) 9 h simulation, and (c) 12 h simulation. The land portion of the Figures are marked with heavier lines. The contour intervals are 1 cm s^{-1}, 5 cm s^{-1} and 10 cm s^{-1}, respectively

(see Fig. 1) around 1900–2000 UTC. This result also agrees with the satellite imagery (Fig. 2b) indicating stronger convection over the east coast at this hour. The eastern boundary of the secondary upward motion zone is now located at about 20 km west of the location predicted at 6 h. The secondary upward motion now occurs over a narrower region with a maximum value of more than 10 cm s^{-1}.

Two upward motion zones are predicted at 12 h as shown in Fig. 8c. Intensity of the upward motion near the east coast is now much weaker as compared to the one near the west coast. Upward motion of about 10 cm s^{-1} extends to about 7 km height over the west coast, but only to about 5 km height over the east coast. Maximum values of the upward motion over the west and east coasts are 100 cm s^{-1} and 35 cm s^{-1}, respectively. The larger downward velocities are now associated with the west coast deep convection. It appears that the secondary upward motion as indicated in Fig. 8a and 8b have merged with the one over the west coast. This merger has obviously caused the deep convection over the west coast at this hour. This result is consistent with the observed strong convective activities near the west coast as indicated in the satellite images (Fig. 2d).

The evolution of turbulent kinetic energy (TKE) e from 6 h to 12 h is shown in Fig. 9a to 9c. The value of e larger than 2 m^2 s^{-2} is confined to within the first 2 km at 6 h as shown in Fig. 9a. Strongest turbulent mixing occurs over the east coast. Turbulent exchange occurs over three regions by 9 h as shown in Fig. 9b. Height of the boundary layer
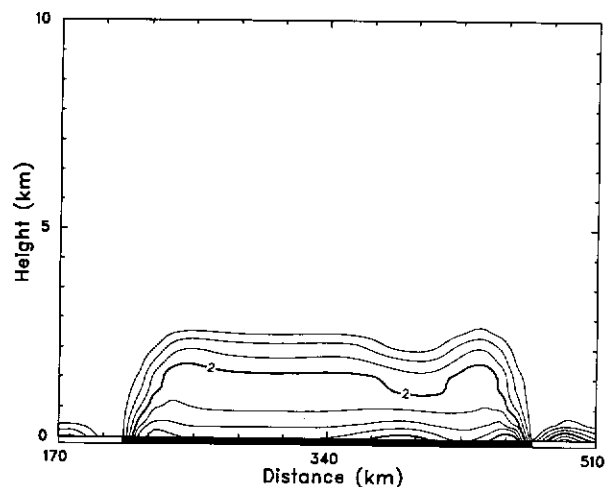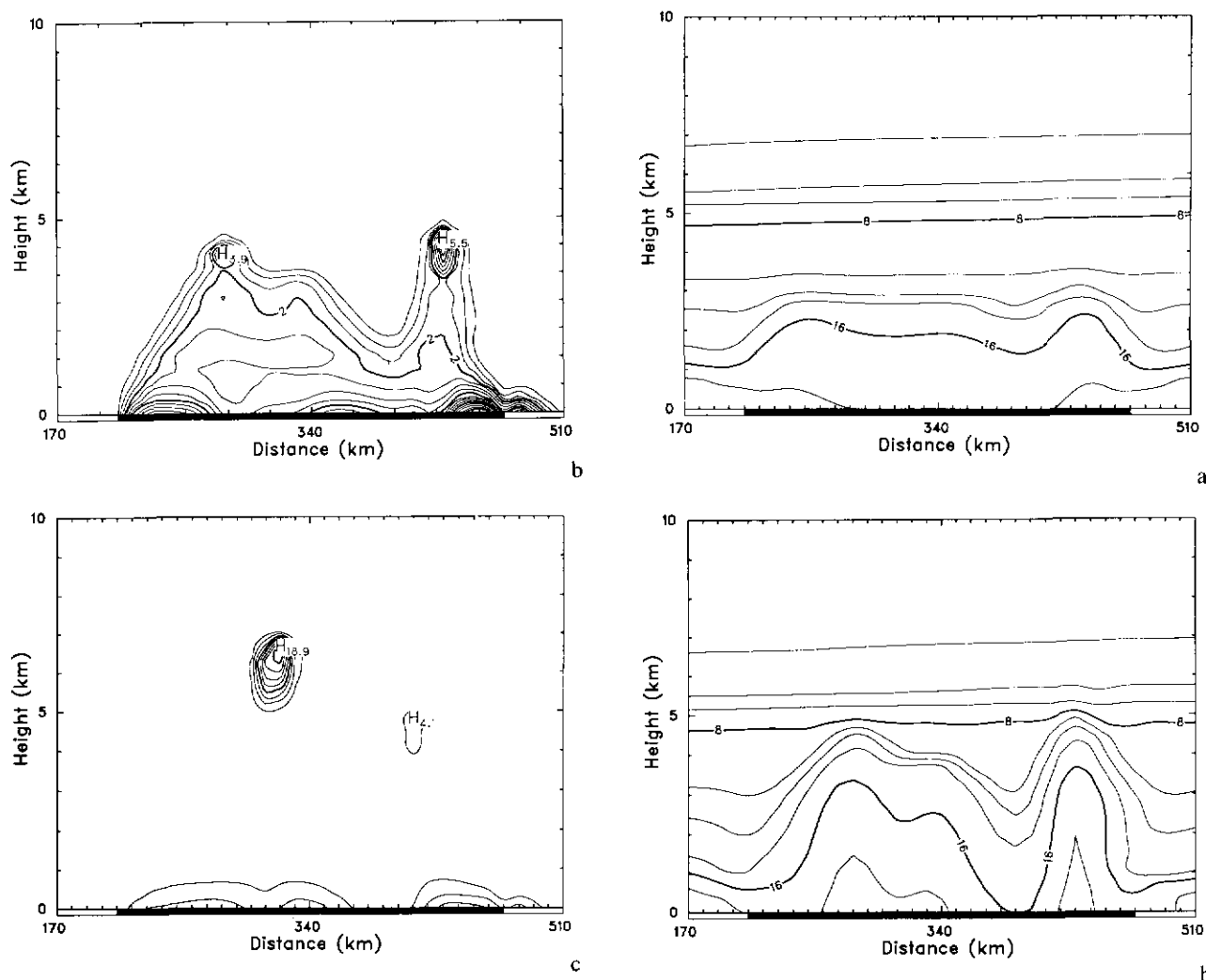

Fig. 9. (Continued)

Fig. 9. Cross sections of the simulated turbulent kinetic energy (in $m^2 s^{-2}$) from EXP1 along line $\overline{AB}$ as indicated in Fig. 4a, at (a) 6 h simulated, (b) 9 h simulation, and (c) 12 h simulation. The land portion of the figures are marked with heavier lines. The contour intervals are $0.5\,m^2 s^{-2}$, $0.5\,m^2 s^{-2}$ and $2\,m^2 s^{-2}$, respectively

(inferred from TKE variation) grew to about 3 km over the west coast and to about 2 km over the east coast. Turbulence over the east coast is still large because of the strong low level convergence near the sea breeze front.

The TKE predicted at 12 h is shown in Fig. 9c. Both the magnitudes and the area of vigorous turbulence decrease as compared to the values at 9 h except for the turbulence associated with the clouds near the west coast at an altitude of about 7 km. The maximum value of the TKE at this height is about $19\,m^2 s^{-2}$ and occurs over an area of about 40 km in hirozontal and about 12 km in the vertical.
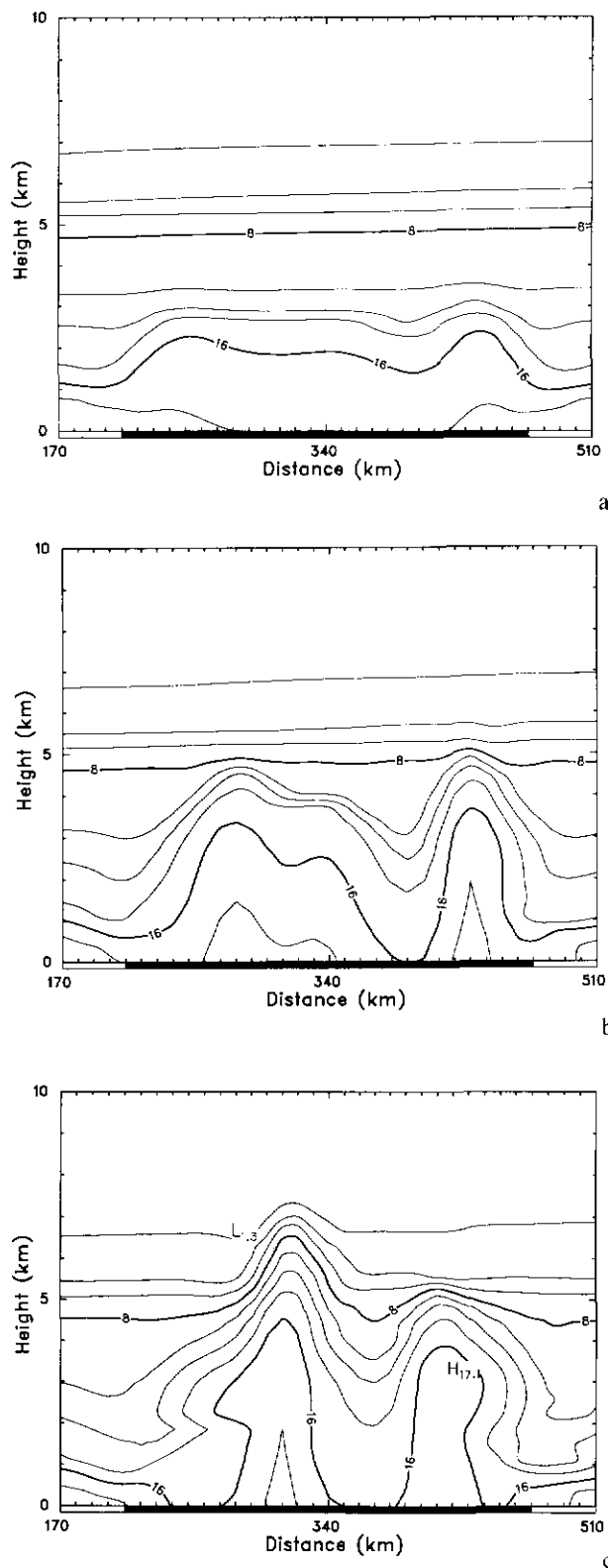
Fig. 10. Cross sections of the simulated water vapor (in $g\,kg^{-1}$) from EXP1 along line AB as indicated in Fig. 4a, at (a) 6 h simulation, (b) 9 h simulation, and (c) 12 h simulation. The land portion of the figures are marked with heavier lines. The contour interval used here is $2\,g\,kg^{-1}$

The 6 h water vapor field is shown in Fig. 10a. The maximum value of the water vapor is about 18 g kg^{-1}. Air is moister over a deeper layer on the land. The main reason for the increase of water vapor over land is believed to be due to turbulent mixing in the boundary layer.

The water vapor field at 9 h is shown in Fig. 10b. More moisture is present over land. The penetration of the moisture to higher levels (about 4 km) is due to turbulent mixing and upward advection. Moisture over the east coast is confined to a narrower region but extends to higher elevations (about 5 km) is consistent with the early afternoon convection.

The 12 h water vapor field shows further penetration of the lower level moist air into higher levels as shown in Fig. 10c. Due to the decrease in turbulent activities at this hour as indicated in Fig. 9c, the transportation of moisture is mainly caused by vertical advection. Since the upward motion is much stronger over the west coast than over the east coast at this hour, the water vapor reaches to about 7 km height over the west coast but only to about 5 km in the east.

No cloud forms at 6 h. Clouds form over both the coasts at 9 h (Fig. 11a). The maximum values of the cloud water are 0.25 g kg^{-1} and 0.11 g kg^{-1} over the east and the west coasts, respectively. The diabatic heating at 9 h (Fig. 11b) shows heating in the cloud region due to condensation and cooling near the cloud boundaries due to evaporation. The cloud water distribution at 12 h shown in Fig. 1c suggests that the cloud formed over the west coast at 9 h is now growing bigger in size and
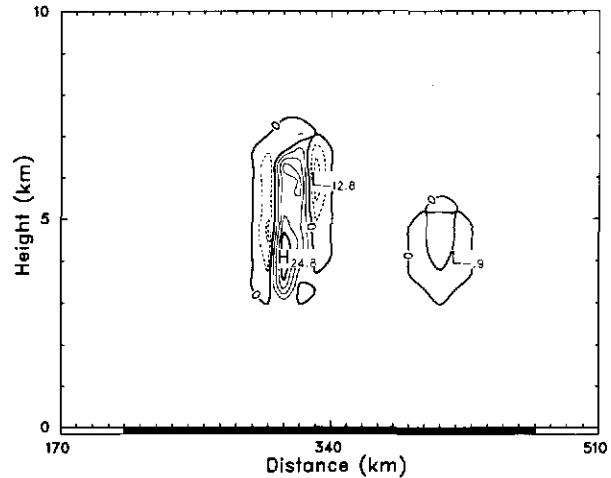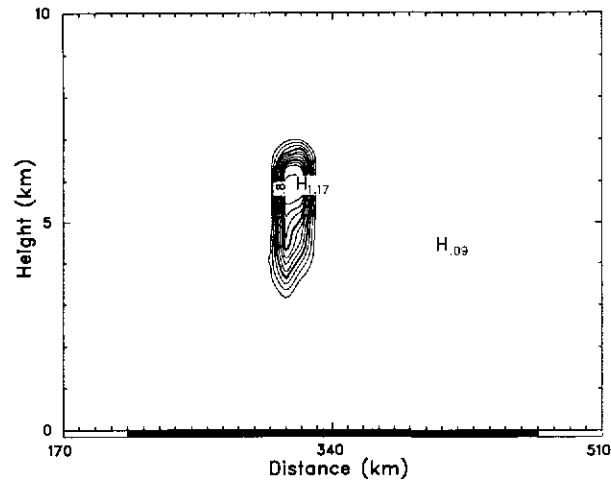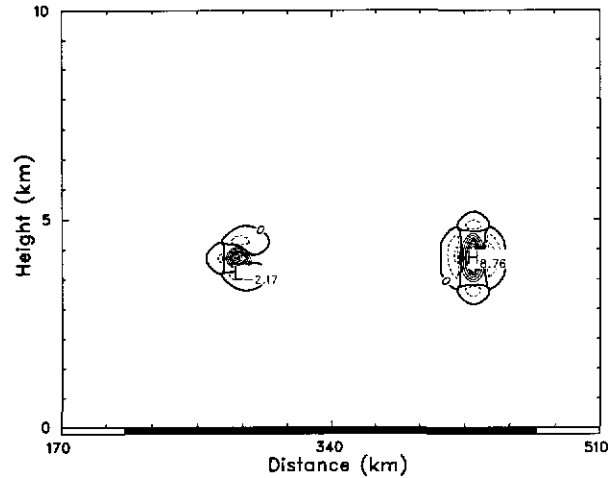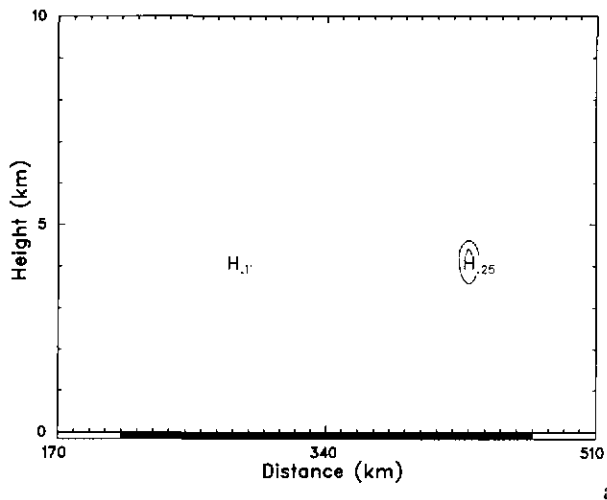

b

c

d

Fig. 11. Cross sections of cloud water and diabatic heating from EXP1 along line AB as indicated in Fig. 4a, for (a) cloud water at 9 h, (b) diabatic heating at 9 h, (c) cloud water at 12 h, and (d) diabatic heating at 12 h. The contour intervals are 0.1 g kg^{-1}, 1 °C hr^{-1}, 0.1 g kg^{-1} and 5 °C hr^{-1}, respectively

a

reaches to about 7 km height. The maximum value of the cloud water is $1.2 \, g \, kg^{-1}$. On the other hand the cloud over the east coast has decayed by this hour. The value of cloud water over the east coast is now less than $0.1 \, g \, kg^{-1}$. The diabatic heating associated with cloud formation at 12 h is given in Fig. 11d. Strong diabatic heating and cooling occur mainly over the west coast with a maximum heating rate of about $25 \, °C \, hr^{-1}$ and a maximum cooling rate of about $13 \, °C \, hr^{-1}$. However, both diabatic heating and cooling rates over the east coast are less than $1 \, °C \, hr^{-1}$. This result is also consistent with the observed stronger convection in the west coast at this hour.
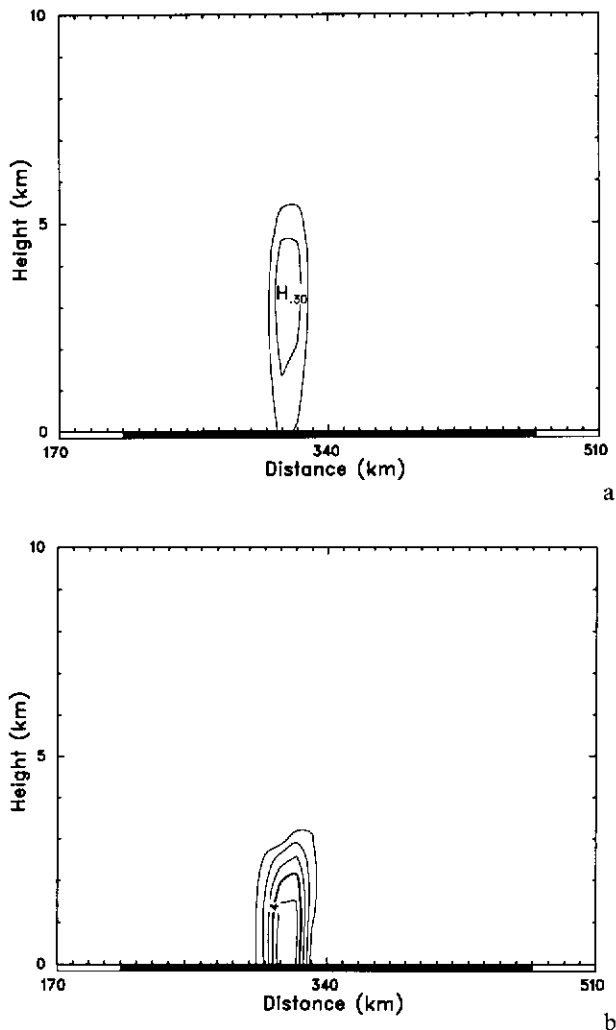

a

b

Fig. 12. Cross sections of rain water and evaporative cooling from EXP1 along line AB as indicated in Fig. 4a, for (a) rain water at 12 h, and (b) evaporative cooling at 12 h. The contour intervals are $0.1 \, g \, kg^{-1}$ for rain water and $1 \, °C \, hr^{-1}$ for evaporative cooling

No rain water is simulated until 11 h. The rain water distribution at 12 h along cross section $\overline{AB}$ is shown in Fig. 12a. Rain water forms only over the west coast. The maximum value of rain water is about $0.3 \, g \, kg^{-1}$ at this cross section. Once the rain water falls out of the cloud into an unsaturated environment, evaporative cooling takes place. The evaporative cooling of rain water at 12 h is given in Fig. 12b. Although the rain water reaches to about 6 km height, the evaporative cooling of rain water occurs only for the first 3 km over the west coast. The reason is that the rain water is mixed with the cloud water above 3 km height (see Fig. 12a and Fig. 11c). The maximum cooling rate is about $5 \, °C \, hr^{-1}$ for this cross section.

4.2 Sensitivity to Ground Surface Moisture

A key element that determines the intensity of the sea breeze circulation is the surface turbulent heat flux. The sensible heat flux is influenced by the surface temperature, and the latent heat flux by the surface soil moisture. Latent heat flux is an important part of the surface energy budget. Differences in the ground surface moisture would have a significant effect on the surface temperature and would affect the sea breeze circulation and consequent convection and precipitation. Two extreme ground moisture conditions are used to test the sensitivity of the surface moisture on the evolution of the sea breeze and the associated convection on 17 July 1991.

The increase of ground temperature is kept to a minimum by the large evaporative cooling when the surface is fully saturated or $W_g = W_{max}$ in Eq. (4). As shown in Fig. 13a, maximum deviation of the ground temperature reaches to only about $7 \, °C$ as compared to about $13 \, °C$ in EXP1 at the same hour. As a consequence, a relatively weak sea breeze is simulated at this hour in EXP2 as indicated by the surface wind distribution in Fig. 13b. The maximum wind speed is only $7.7 \, m \, s^{-1}$. However, the model predicts a rapid increase in the ground temperature and very strong sea and lake breezes when a dry condition is prescribed for the surface or $W_g = 0$ in Eq. (4) for EXP3. The maximum ground temperature in this case increases to about $50 \, °C$ for EXP3 as shown in Fig. 13c. The simulated maximum wind speeds at 6 h increases to $24.3 \, m \, s^{-1}$ in EXP3 as shown in Fig. 13d.

a

b

c

d

Fig. 13. (a) As in Fig. 5a except that this is from EXP2. The contour interval is 1 °C. (b) As in Fig. 4a except that this is for EXP2. The maximum wind speed is about 7.7 m s^{-1}. (c) As in Fig. 5a and Fig. 13a except that this is from EXP3. The contour interval is 1 °C. (d) As in Fig. 4a and Fig. 13b except that this is from EXP3. The maximum wind speed is 24.3 m s^{-1}

Contours of GTDs, and wind vectors for EXP2 at 9 h are shown in Fig. 14a and 14 b, respectively. Maximum ground temperature increases less than 1 °C in 3 h. Maximum wind speed increases to 9.3 m s^{-1} at this hour. The sea breeze circulation at this hour is weaker as compared to the one in EXP1. But the wind field does indicate some similar features simulated in EXP1 such as the
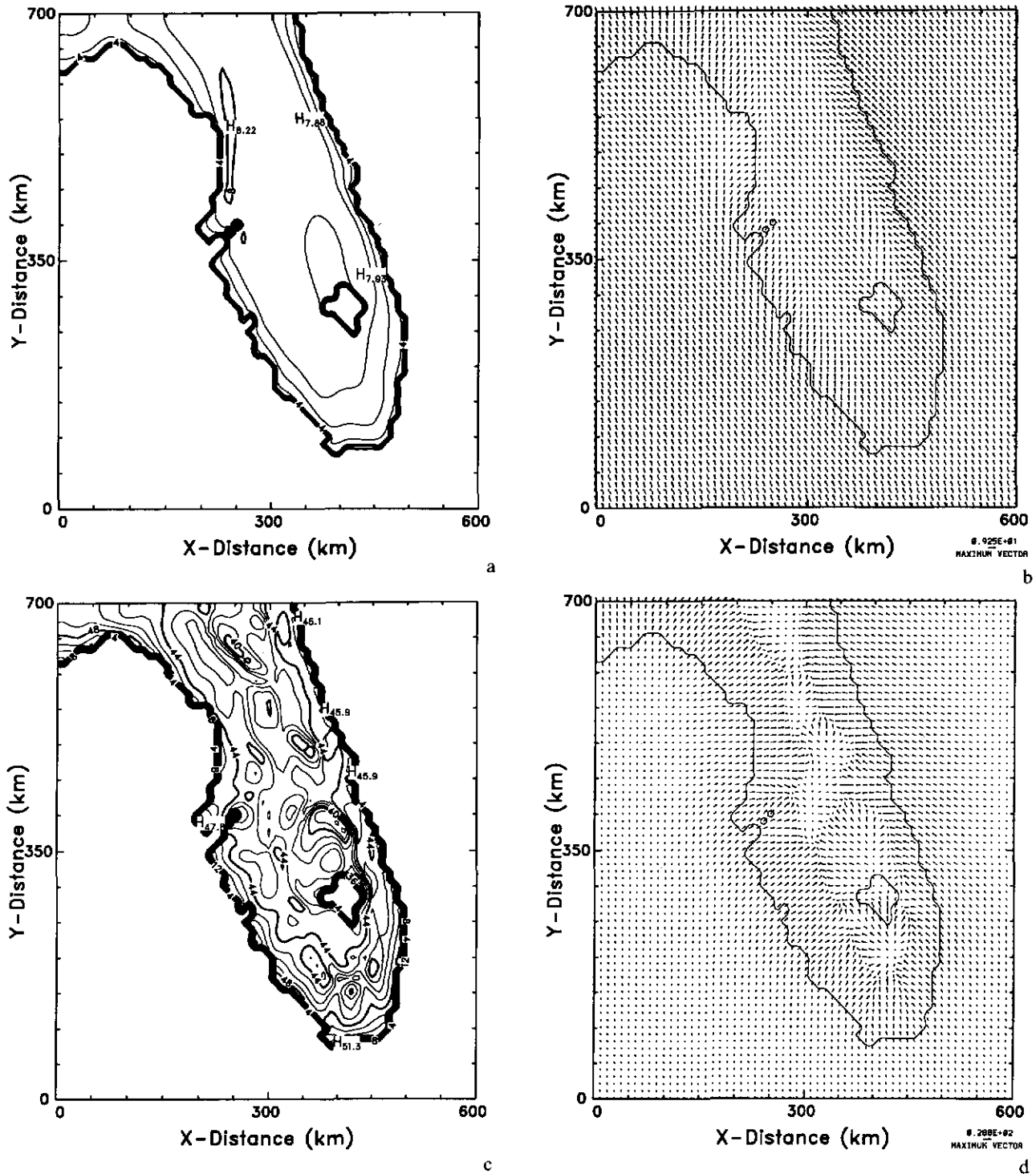
Fig. 14. (a) As in Fig. 5b except that this is from EXP2. The contour interval is 1 °C. (b) As in Fig. 4b except that this is for EXP2. The maximum wind speed is about 9.3 m s^{-1}. (c) As in Fig. 5b and Fig. 14a except that this is from EXP3. The contour interval is 1 °C. (d) As in Fig. 4b and Fig. 14b except that this is from EXP3. The maximum wind speed is 28.8 m s^{-1}

convergence zones over the central east and north-west coasts as shown in Fig. 14b. For comparison, contours of GTDs, and wind vectors for EXP3 are shown in Fig. 14a and 14b, respectively. The

ground temperature deviation at 9 h is still very large. Small ground temperature deviations at 9 h are associated with the low wind speeds near the surface at this hour as indicated in Fig. 14d. The

maximum wind speed at this hour is 28.8 m s^{-1}. The sea breeze extends further inland over the west coast than over the east coast, especially over central Florida. As mentioned previously, the

Coriolis force plays an important role in preventing the advance of the sea breeze further inland over the east coast for EXP1. The lake breeze, on the other hand, appears to be the main factor in
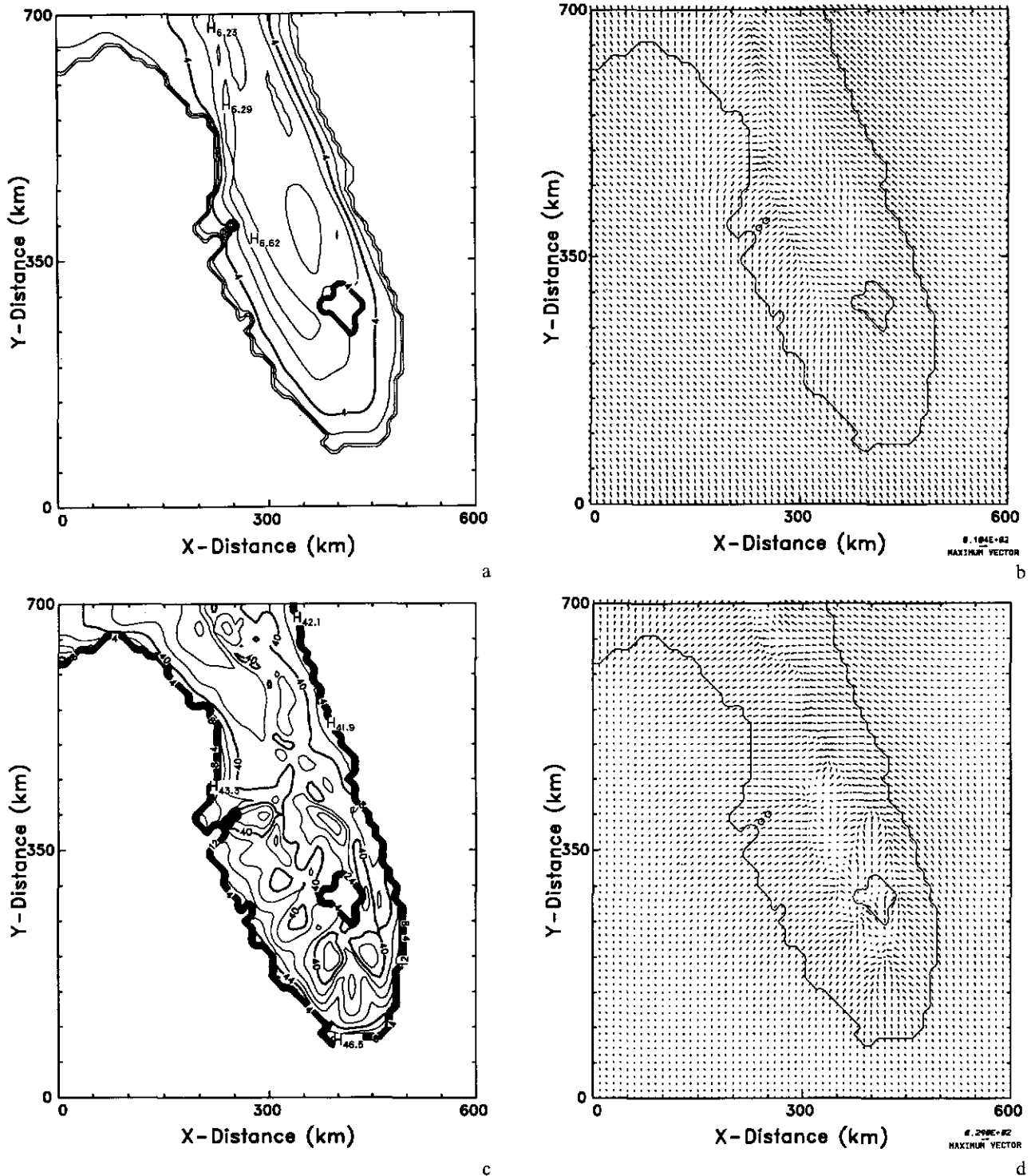

a

b

c

d

Fig. 15. (a) As in Fig. 5c except that this is from EXP2. The contour interval is 1 °C. (b) As in Fig. 4c except that this is for EXP2. The maximum wind speed is about 10.4 m s^{-1}. (c) As in Fig. 5c and Fig. 15a except that this is from EXP3. The contour interval is 1 °C. (d) As in Fig. 4c and Fig. 15b except that this is from EXP3. The maximum wind speed is 29 m s^{-1}

preventing the advance westwards of the sea breeze due to the opposing directions of the sea and lake breezes in all the three experiments.

At 12 h, maximum value of the ground temperature deviation in EXP2 decreases to about 6.6 °C as indicated in Fig. 15a. Higher values are mainly over the west coast. The relatively cool region northwest of lake Okeechobee is believed to be a result of the cold air advection from the lake. The maximum wind speed at 12 h is only about 10.4 m s^{-1} for EXP2. Stronger convergence occurs mainly over the west coast as shown in Fig. 15b. Since the sea breeze circulation in EXP2 is relatively weak, the ambient wind contains a larger portion of the total wind. The sea breeze fronts generated by the two coasts never merge in EXP2. Figure 15c shows the ground temperature deviation at 12 h for EXP3. The ground temperatures are several degrees colder at 12 h than at 9 h, but still very warm as compared to the ones in both EXP1 and EXP2. The two sea breeze fronts advance further inland and merge in some regions as indicated in Fig. 15d.

When the ground is kept saturated during the integration, the increase of surface temperature will increase the amount of the latent heat flux from the ground into the atmosphere. The latent heat flux from the ground, however, has a cooling effect on the ground temperature. The decrease of ground temperature tends to generate less latent heat flux from the ground into the atmosphere. When the ground is kept dry during the integration, on the other hand, the ground temperature increases rapidly. The rapid increase in ground temperature is because there is no latent heat flux from the ground into the atmosphere for dry soil. The change in ground temperature in Eq. (1) is now balanced only by the net radiation and the sensible heat flux. The rapid increase of the ground temperature will in general release more sensible heat into the atmosphere, which in turn produces stronger sea breeze circulation.

Based on the comparison of ground temperature deviation and near surface wind fields, we find that the ground moisture plays a very important role in determining the ground temperature and the wind fields. The results suggest that both ground temperature and wind fields respond to the ground moisture conditions in a monotonic manner. However, further examination of the precipitation fields reveals subtle relationships between precipitation and ground moisture conditions. Figure 16a and 16b show the 12 h accumulated precipitation for EXP2 and EXP3, respectively. Precipitation occurs between 9 h and 12 h with a maximum
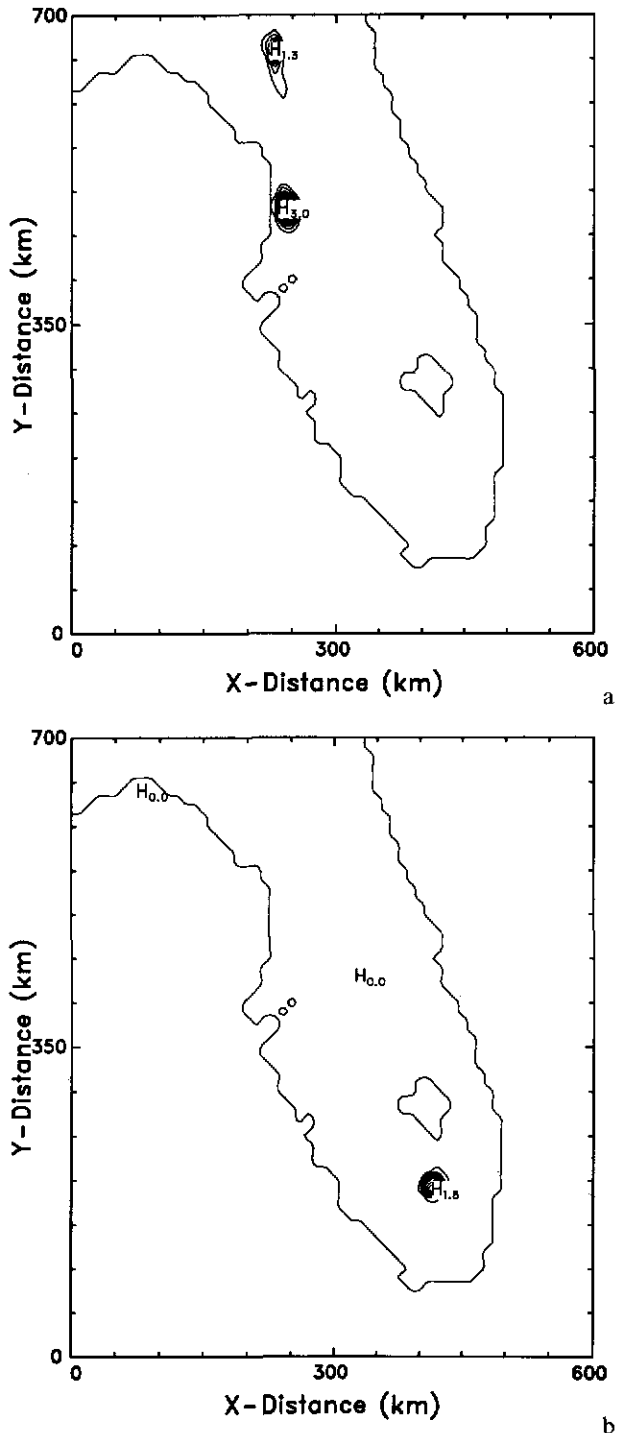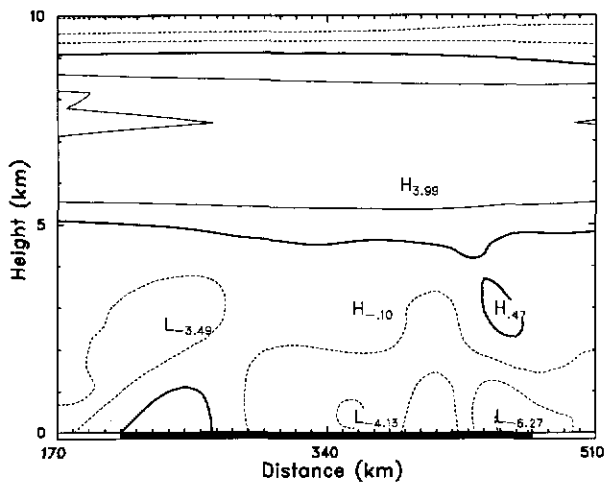

Fig. 16. (a) As in Fig. 6 except that this is from EXP2. The unit is in mm and the contour interval is 0.2 mm. (b) As in Fig. 6 and Fig. 16a except that this is from EXP3. The unit is in cm and the contour interval is 0.2 cm
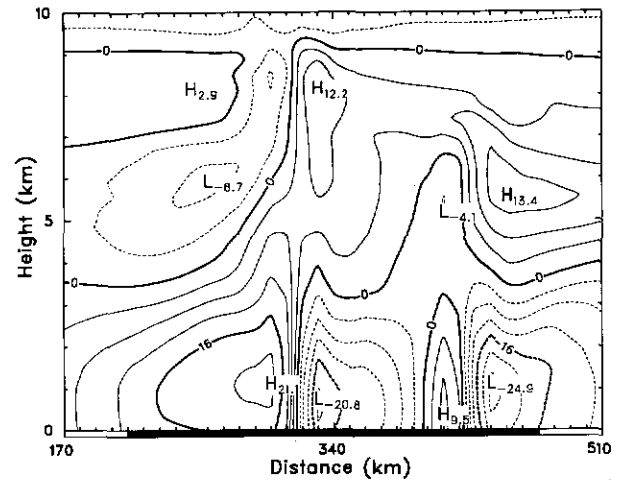
amount of about 0.3 cm in EXP2 as indicated in Fig. 16a. The precipitation pattern of EXP2 is close to the one in EXP1 over central and northern Florida, but the amount of precipitation is an order of magnitude smaller than the one for EXP1 (see Fig. 6). In EXP3, however, the precipitation occurs between 6 h and 9 h with a maximum amount of about 1.8 cm over a location 70 km south of lake Okeechobee (Fig. 16b). The predicted precipitation from the control experiment (EXP1) is far better than the ones from EXP2 and EXP3. No simple relationship seems to exist between the amount of accumulated precipitation and the ground moisture conditions.

The relatively small amount of precipitation simulated in EXP2 is because of weak convection caused by weak sea breeze circulation in EXP2. As discussed previously, the weak sea breeze is caused by the assumption of saturated ground. The precipitation that occurred in EXP3 is the result of very strong convection due to strong sea breeze convergences. The moisture used to produce the precipitation in EXP3 is from the initial condition, since there is no moisture flux from the ground into the atmosphere.

To further demonstrate the effect of ground moisture conditions on the sea breeze circulation and the associated convection, a vertical cross section is examined. For consistency, the cross sections discussed in the following is along the line $\overline{AB}$ as indicated in Fig. 4a. The u-components of wind for EXP2 and EXP3 at 9 h are shown in Fig. 17a and 17b, respectively. The sea breeze circulation is much stronger and penetrates ap-
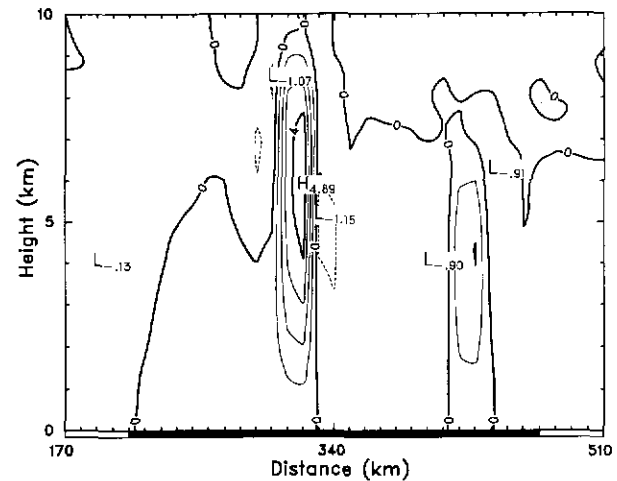

b
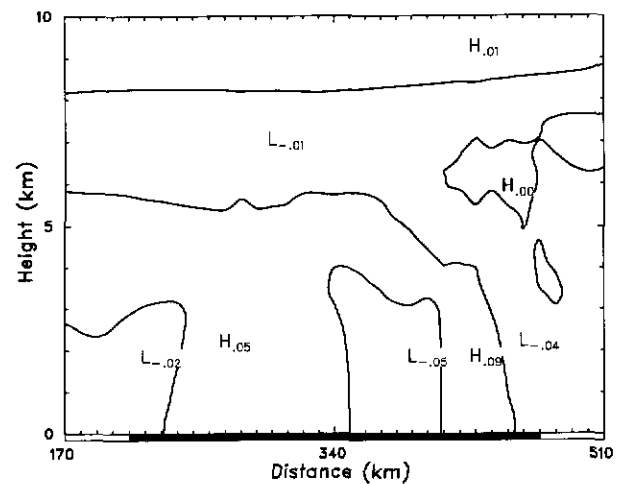
c

d

Fig. 17. (a) As in Fig. 7b except that this is from EXP2. The contour interval is $2 \, \text{m s}^{-1}$. (b) As in Fig. 7b and Fig. 17a except that this from EXP3. The contour interval is $4 \, \text{m s}^{-1}$. (c) As in Fig. 8b except that this is from EXP2. The contour interval is $0.1 \, \text{m s}^{-1}$. (d) As in Fig. 8b and Fig. 17c except that this is from EXP3. The contour interval is $1 \, \text{m s}^{-1}$

a

proximately 50 km further inland in EXP3 than in EXP2 as indicated in Fig. 17a and 17b over the west coast. The maximum value of westerly wind component within the first km in EXP2 is less than $2 \, m \, s^{-1}$ (see Fig. 17a) as against $21 \, m \, s^{-1}$ in EXP3 (see Fig. 17b). The maximum values of easterly wind component are about $6 \, m \, s^{-1}$ and $25 \, m \, s^{-1}$ in EXP2 and EXP3, respectively. The w-components of wind for EXP2 and EXP3 at 9 h are shown in Fig. 17c and 17d, respectively. Very weak convection ($w \leqslant 0.09 \, m \, s^{-1}$) is present near both the coasts in EXP2 as shown in Fig. 17c. The values of upward motions, more than $2 \, m \, s^{-1}$ and $4 \, m \, s^{-1}$ (strong convection) are present over the east and the west coasts, respectively. The differences in the u- and w-components between EXP2 and EXP3 are mainly caused by the differences in the ground moisture conditions.

5. Summary and Conclusions

In this study, evolution of a sea breeze event and the associated convection and subsequent precipitation observed during the 1991 Convection and Precipitation Electrification (CaPE) experiment are simulated using a fully-compressible three-dimensional non-hydrostatic numerical model. The inclusion of surface energy and moisture budget allows us to simulate the diurnal cycle of the ground surface temperature and wetness. A sounding obtained from Orlando, Florida at 1110 UTC 17 July 1991 as part of the CaPE is used for initialization. The control experiment reasonably reproduces the evolution of the sea breeze circulation, convection and precipitation observed on this day. Lake Okeechobee appears to have a significant impact on the circulations based on the model results.

The effects of surface moisture conditions are examined using two sensitivity tests. They assume the ground surface to be saturated and dry, respectively. The surface moisture is found to have significant effects on the atmosphere. Slow increase of the surface temperature is predicted when more ◄moisture is available at the surface. Drier ground surface causes stronger circulations and more turbulent mixing. The amount of predicted precipitation is found to be very sensitive to the surface moisture conditions.

This study suggests that the ground surface

moisture plays an important role in the initiation and the maintenance of the convective clouds and precipitation. To correctly simulate the sea breeze and the associated rainfall, inclusion of surface energy and moisture budget in the model is necessary. Future work would involve incorporation of a vegetation scheme in the model to account for the land use pattern.

References

Arakawa, A., Lamb, V. R., 1977: Computational design of the UCLA general circulation model. *Methods in Computational Physics.* Vol. 17, New York: Academic Press, pp. 173–265.

Bougeault, P., 1987: A qualification study of the French Weather Service limited-area-model, pp. 51–52. In: *Extended Abstracts. Third Conference on Mesoscale Processes.* American Meteorological Society.

Deardorff, J. W., 1980: Stratocumulus-capped mixed layers derived from a three-dimensional model. *Bound.-Layer Meteor.,* 18, 495–527.

Hodur, R. M., 1993: Development and testing of the Coupled Ocean/Atmospheric Mesoscale Prediction System (COAMPS). NRL/MR/7533-93-7213, Naval Research Laboratory, 84 pp. [Available from the Naval Research Laboratory, Monterey, CA 93943-3502].

Klemp, J., Wilhelmson, R., 1978: The simulation of three-dimensional convective storm dynamics. *J. Atmos. Sci.,* 35, 1070–1096.

Louis, J. F., Tiektke, M., Geleyn, J. F., 1979: A parametric model of vertical eddy fluxes in the atmosphere. *Bound. Layer Meteor.,* 17, 187–202.

Louis, J. F., Tiektke, M., Geleyn, J. F., 1982: A short history of the operational PBL-parameterization at ECMWF. Workshop on Planetary Boundary Parameterization, ECMWF, Reading, pp. 59–79. [Available from the European Center for Medium-Range Forecasts, Shinfield Park, Reading RG2 9Ax, U.K.]

Mahfouf, J. F., Richard, E., Mascart, P., Nickerson, E. C., Rosset, R., 1987: A comparative study of various parameterizations of the planetary boundary in a numerical mesoscale model. *J. Climate Appl. Meteor.,* 26, 1671–1695.

McCumber, M. C., 1980: A numerical simulation of the influence of heat and moisture fluxes upon mesoscale circulations. Ph.D. dissertation, Dept. of Environmental Sciences, University of Virginia.

Mellor, G., Yamada, T., 1974: A hierarchy of turbulence closure models for planetary boundary layers. *J. Atmos. Sci.*, **31**, 1791–1806.

Nicholls, M. E., Pielke, R. A., Cotton, W. R., 1991: A two-dimensional numerical investigation of the interaction between sea breezes and deep convection over the Florida peninsula. *Mon. Wea. Rev.*, **119**, 298–323.

Orlanski, I., 1976: A simple boundary condition for unbounded hyperbolic flows. *J. Comput. Phys.*, **21**, 251–269.

Pielke, R. A., 1974: A three-dimensional numerical model of the sea breezes over south Florida. *Mon. Wea. Rev.*, **102**, 115–139.

Robert, A. J., 1966: The investigation of a low order spectral form of the primitive meteorological equations. *J. Meteor. Soc. Japan*, **44**, 237–245.

Robert, A. J., 1969: The integration of a spectral model of the atmosphere by the implicit methods. Proc. of the WMO/ IUGG Symp. on NWP, Tokyo, Japan Meteor. Agency, **VII**, 19–24.

Rutledge, S. A., Hobbs, P. V., 1983: The mesoscale and microscale structure of organization of clouds and precipitation in midlatitude cyclones. VIII: A model for the "seeder-feeder" process in warm-frontal rainbands. *J. Atmos. Sci.*, **40**, 1185–1206.

Smagorinsky, J., 1963: General circulation experiments with the primitive equations: 1. The basic experiment. *Mon. Wea. Rev.*, **91**, 99–164.

Tapp, M. C., White, P. W., 1976: A nonhydrostatic mesoscale model. *Quart. J. Roy. Meteor. Soc.*, **102**, 227–296.

Williams, S. F., Caesar, K., Southwick, K., 1992: The Convection and Precipitation Electrification (CaPE). *Operations Summary and Data Inventory.* Office of Field Project Support, National Center for Atmospheric Research, Boulder, Colorado.

Xu, L., Raman, S., Madala, R. V., 1992: A review of non-hydrostatic numerical models for the atmosphere. First World Congress of Nonlinear Analysis, Tampa, Florida USA. Nonlinear World, Walter de Gruyter, New York, (in press).

Authors' addresses: L. Xu, S. Raman, Department of Marine Earth and Atmospheric Sciences, North Carolina State University, Raleigh, NC 27695-8208, U.S.A.; R. V. Madala, Naval Research Laboratory, Washington, D.C. 20375, U.S.A.; R. Hodur, Naval Research Laboratory, Monterey, CA 93943, U.S.A.